

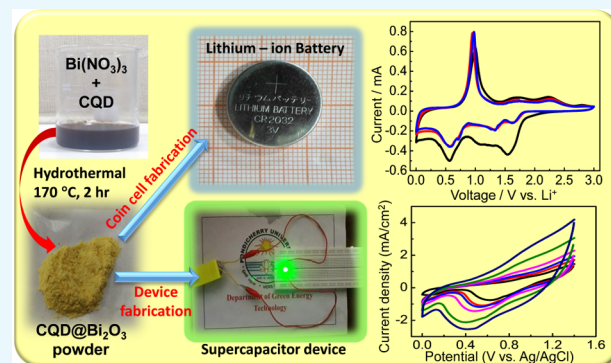
Carbon Quantum Dot-Anchored Bismuth Oxide Composites as Potential Electrode for Lithium-Ion Battery and Supercapacitor Applications

Arul Prasath, Mattath Athika, Ezhumalai Duraisamy, Arumugam Selva Sharma,^{iD} Vaithiyanathan Sankar Devi, and Perumal Elumalai^{*ID}

Electrochemical Energy and Sensors Laboratory, Department of Green Energy Technology, Madanjeet School of Green Energy Technologies, Pondicherry University, Puducherry 605014, India

S Supporting Information

ABSTRACT: The present investigation elucidates a simple hydrothermal method for preparing nanostructured bismuth oxide (Bi_2O_3) and carbon quantum dot (CQD) composite using spoiled (denatured) milk-derived CQDs. The formation of the CQD– Bi_2O_3 composite was confirmed by UV-vis absorption, steady-state emission, and time-resolved fluorescence spectroscopy studies. The crystal structure and chemical composition of the composite were examined by X-ray diffraction, Fourier transform infrared spectroscopy, Raman spectroscopy, and thermogravimetric analysis. The surface morphology and the particle size distribution of the CQD– Bi_2O_3 were examined using field emission scanning electron microscope and high-resolution transmission electron microscope observations. As an anode material in lithium-ion battery, the CQD– Bi_2O_3 composite exhibited good electrochemical activity and delivered a discharge capacity as high as 1500 mA h g^{-1} at 0.2C rate. The supercapacitor properties of the CQD– Bi_2O_3 composite electrode revealed good reversibility and a high specific capacity of 343 C g^{-1} at 0.5 A g^{-1} in 3 M KOH . The asymmetric device constructed using the CQD– Bi_2O_3 and reduced graphene oxide delivered a maximum energy density of 88 Wh kg^{-1} at a power density of 2799 W kg^{-1} , while the power density reached a highest value of 8400 W kg^{-1} at the energy density of 32 Wh kg^{-1} . The practical viability of the fabricated device is demonstrated by glowing light-emitting diodes. It is inferred that the presence of conductive carbon network has significantly increased the conductivity of the oxide matrix, thereby reducing the interfacial resistance that resulted in excellent electrochemical performances.



INTRODUCTION

In recent years, spike in the industrial activities and the quest for a sophisticated lifestyle have resulted in a huge demand for energy. Currently, most of the energy demands are met by combustion of nonrenewable fossil fuels that has resulted in the emission of toxic greenhouse gases into the environment.^{1,2} Owing to the shortage of the fossil fuel reserves and the imminent threat of global warming, the pursuit for developing new technologies for clean energy production has become indispensable. The use of renewable resources such as solar and wind power could mitigate several energy and environmental issues. As a result, reliance on renewable resources is on the rise, and subsequently, there is an increasing need to store this energy for longer duration.^{1–5} Electrochemical energy-storage devices such as batteries and supercapacitors (SCs) offer an attractive way to store energy obtained from renewable resources for sufficient time, to achieve a sustainable and pollution-free environment.^{1–5}

Among the various battery technologies, lithium-ion battery (LIB) is considered as a viable energy-storage device to fulfill

the current energy needs of the consumer electronics.⁶ LIB possesses several unique features such as high energy density, high voltage, and reasonably longer lifespan. A typical commercial LIB consists of an anode material made of graphite (theoretical capacity: 372 mA h g^{-1}) and lithium transition-metal oxide (e.g., doped LiCoO_2 or LiFePO_4 ; theoretical capacity: 170 mA h g^{-1}) as cathode material. A nonaqueous solution of LiPF_6 in ethylene carbonate (EC) and diethylene carbonate is used as electrolyte.^{7–10} Despite the appreciable performances of the LIBs in low-power portable electronic gadgets, large improvement in electrode materials has to be made to achieve higher energy density, larger gravimetric/volumetric capacity, and better cycling performances.^{6–10} In addition, to meet the future needs of electric vehicles and grid-scale energy storage, researchers have devoted arduous efforts to develop alternative anode materials

Received: December 13, 2018

Accepted: February 20, 2019

Published: March 6, 2019



for the LIBs to replace the current low-capacity graphitic anode that works solely on the basis of the intercalation process.^{6,9} In particular, metal oxides and sulfides have attracted significant attention due to their stable chemical states and high theoretical capacity in the range of 600–1000 mA h g⁻¹, which is significantly higher than that of the conventional graphite anode material.^{6–10}

Recently, bismuth oxide (Bi_2O_3), owing to its high theoretical capacity of 690 mA h g⁻¹, has been proposed as a potential anode material for LIB.¹¹ For instance, Fiordiponti et al. examined Li-storage features of Bi_2O_3 and reported a capacity of 660 mA h g⁻¹.¹² Nearly two decades later, Li et al. grew nanostructured Bi_2O_3 on nickel foam using a polymer-assisted solution approach and demonstrated its use as an anode material in LIBs with a capacity of 668 mA h g⁻¹.¹³ Nevertheless, the cycling stability was limited and required further improvements. To realize higher capacity and long cycle life, various composites have been proposed. For example, Li et al. demonstrated the preparation of macroporous Bi_2O_3 using poly(methyl methacrylate) spheres as colloidal crystal template and observed a reversible capacity of 500 mA h g⁻¹ at 0.2C rate.¹⁴ Fang et al. synthesized the Bi_2O_3 /graphene composite and reported significant enhancement in capacity with cycling stability.¹⁵ The same research group prepared the polypyrrole-coated Bi_2O_3 to improve the electron transport properties and used it in the LIB.¹⁶ Quite recently, Bi_2O_3 /reduced graphene oxide (rGO) nanocomposite has been generated via chemical bonding as an anode material for LIB and shown to exhibit enhanced electrochemical performance with appreciable capacity of 900 mA h g⁻¹ at 0.1C rate.¹⁷ In another case, Liu et al. designed Bi_2O_3 – Bi_2S_3 heterostructure through partial sulfurization of Bi_2O_3 nanosheets and demonstrated a coulombic efficiency of 83.7%.¹⁸

In contrast to LIBs, supercapacitors can store charge by either nonfaradic or fast faradic reactions at the electrode surface.^{1,4} It is well known that a typical supercapacitor releases energy rapidly due to its ability to provide high power, long cycle life, and fast charge–discharge processes. Subsequently, the performance of the supercapacitor is highly dependent on the nature of the electrode material in terms of its morphology, size, porosity, etc.^{1,4} Recently, nanostructured Bi_2O_3 has been also examined as electrode material for supercapacitor application.^{1,4,19,20} For example, Li et al. prepared a free-standing nanocomposite of Bi_2O_3 –carbon nanofiber electrode by electrospinning and reported a capacitance of 50 F g⁻¹ for the asymmetric supercapacitor with an energy density of 25 Wh kg⁻¹ at a power density of 786 W kg⁻¹.²¹ Shinde et al. showed that the Bi_2O_3 –Ni-foam-based asymmetric supercapacitor device achieved a high capacitance of 557 F g⁻¹ with an energy density of 80 Wh kg⁻¹.²² Gujar et al. electrochemically deposited Bi_2O_3 thin-film electrode for supercapacitor to exhibit high electrochemical reversibility.²³ Tong's group reported the preparation of Bi_2O_3 nanobelts, which exhibited a specific capacitance of 250 F g⁻¹.²⁴

We have currently reported that the metal-oxide-embedded carbon matrix could facilitate charge and ion transports, leading to improved electrochemical performance for lithium-ion battery and supercapacitor applications.²⁵ Recently, carbon quantum dots (CQDs) and graphene quantum dots have found their uses in several energy-storage applications, namely, supercapacitors and Li- and Na-ion batteries.^{26,27} In our recent work, we have established that the CQDs present in the MnO_2 nanocomposite improved the accessibility of the charged ions

and facilitated efficient charge transport during the charge–discharge processes.²⁸ To the best of our knowledge, there have been no reports on the CQD-embedded nanostructured Bi_2O_3 for energy-storage applications. Thus, in the present study, we have endeavored CQD-mediated synthesis of nanostructured Bi_2O_3 by a simple hydrothermal method and evaluated its electrochemical performances in LIBs and supercapacitors.

RESULTS AND DISCUSSION

Spectral Characterizations of CQD– Bi_2O_3 . Figure 1a shows the absorption profile of the aqueous dispersion of

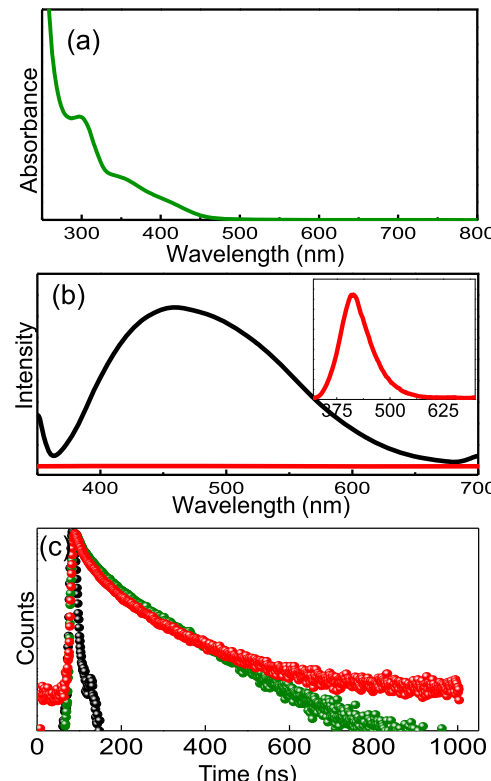


Figure 1. (a) Absorption spectra of aqueous dispersion of the CQD– Bi_2O_3 composite. (b) Steady-state and (c) time-resolved fluorescence profiles recorded for the pristine CQD and the CQD– Bi_2O_3 composite. Inset: Enlarged view of the emission profile of the CQD– Bi_2O_3 composite.

CQD– Bi_2O_3 recorded in the wavelength range of 200–800 nm. It is obvious from Figure 1a that the UV–vis absorption spectral response of CQD– Bi_2O_3 exhibits a broad band in the range of 350–450 nm, which is attributed to the intrinsic band gap absorption of the Bi_2O_3 . It has been reported that the band structure of the Bi_2O_3 is composed of Bi6p atomic orbitals, which are separated into occupied and unoccupied parts.^{29,30} The former hybridizes with the O2p band and contributes to the valence band, while the latter is the main component for the conduction band, thereby leading to the formation of narrow band gap in Bi_2O_3 .^{29,30} Interestingly, the distinctive yellow color of the as-prepared CQD– Bi_2O_3 complements the observed broad absorption band. The strong band centered at 290 nm is attributed to the π – π^* transition of the graphitic structure of the CQDs.²⁸ This clearly indicates that the CQD has been embedded inside the grains of Bi_2O_3 . Liu et al. reported a similar optical absorption behavior in the case of

Bi_2O_3 –rGO composite, in which the band in the range of 300–400 nm is attributed to Bi_2O_3 and a weak band at 268 nm is ascribed to the excitation of π -plasmon of the graphitic structure.³¹ To substantiate the formation of composite, the emission spectral profiles of the CQD and the CQD– Bi_2O_3 composite were recorded and the resulting spectra are displayed in Figure 1b. It is seen that the CQD dispersion exhibits an emission maximum at 425 nm upon excitation at 360 nm. Undoubtedly, in the case of the yellow-colored CQD– Bi_2O_3 dispersion, the emission intensity is quenched drastically with a very weak fluorescence. The formation of weakly fluorescent CQD is attributed to the adsorption of the CQD onto the surface of the formed Bi_2O_3 grains. Such quenching behavior has been reported for the CQD–metal oxide composites.^{27,28}

Time-resolved fluorescence spectroscopy analysis was carried out to delineate the exact quenching mechanism in the CQD– Bi_2O_3 composite. Figure 1c shows the decay profiles of CQD and the CQD– Bi_2O_3 composite. It is apparent from the figure that the decay profiles are best fitted to a triexponential decay curve with average lifetimes of 8.96 and 8.26 ns, respectively. The negligible difference in the fluorescence lifetimes of the CQD and the CQD– Bi_2O_3 composite clearly suggests the formation of nonfluorescent ground-state complex and involvement of static quenching mechanism.³² It is well known that the formation of a ground-state complex between the fluorophore and metal oxide materials cannot induce changes in the fluorescence lifetimes of the fluorophore.³³ Thus, it is believed that the observed emission quenching in the case of the CQD– Bi_2O_3 composite is primarily due to the static quenching mechanism. Moreover, this inference is consistent with the steady-state emission studies. From the absorption, emission, and time-resolved spectral analyses, it can be inferred that the hydrothermal treatment of the bismuth nitrate in aqueous CQD dispersion resulted in the formation of the CQD– Bi_2O_3 composite.

Crystal Structure and Morphology. The crystal structure of the as-prepared CQD– Bi_2O_3 composite was identified by X-ray diffraction (XRD) analysis, and the resultant XRD pattern is displayed in Figure 2a. It is obvious that the XRD pattern of the sample consists of well-defined characteristic diffraction peaks of Bi_2O_3 and carbon. The peaks located at 11.21, 14.12, and 23.31° pertaining to CQD could be indexed to the standard card of carbon (PDF # 46-0870).³⁴ The set of other Bragg peaks at 28.81, 31.23, 33.52, 47.08, and 54.93° are indexed to the (201), (002), (220), (222), and (203) Bragg planes of Bi_2O_3 , respectively. The obtained Bragg peaks are in good agreement with the JCPDS PDF # 65-1209.³⁵ In addition, sharp Bragg peaks with narrow full width at half-maximum imply large grain size and high crystallinity of the sample. During the formation of the CQD– Bi_2O_3 composite, the ultrafine CQD seems to be agglomerated into the larger grains. It has been reported earlier that the Bragg peaks of the Bi_2O_3 obtained using PMMA template synthesis were broad owing to the ultrafine grain size of the material.¹⁴ In a recent report, Deng et al. reported the nearly amorphous nature of the Bi_2O_3 /rGO nanocomposite.¹⁷ Undoubtedly, in the present instance, the presence of sharp Bragg peaks for Bi_2O_3 clearly indicates its highly crystalline nature.

The chemical composition and the surface functional groups of the as-prepared CQD– Bi_2O_3 were investigated by FT-IR and Raman spectral analyses. The FT-IR profile of the CQD– Bi_2O_3 displayed in Figure 2b exhibits a band at 3386 cm^{-1} ,

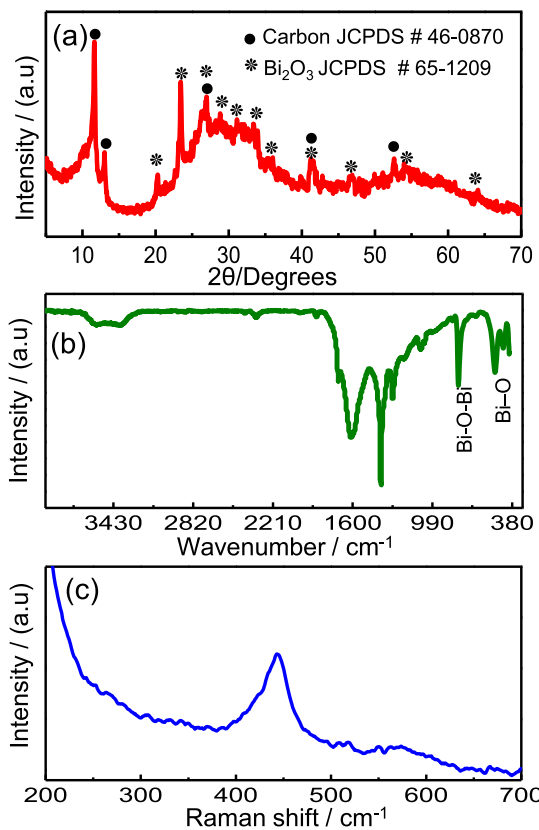


Figure 2. (a) XRD, (b) Fourier transform infrared (FT-IR), and (c) Raman spectral profiles of the CQD– Bi_2O_3 composite.

which is attributed to O–H and N–H stretching vibrations. The sharp bands centered at 1612 and 1375 cm^{-1} are ascribed to C–O stretching and C–H bending vibrations, respectively. All of these peaks are indicative of the presence of the CQD in the Bi_2O_3 sample.²⁸ The peaks located at 464 and 510 cm^{-1} are characteristic of Bi–O vibrations, which is in agreement with the previous reports.³⁵ As shown in Figure 2c, the Raman spectrum of the CQD– Bi_2O_3 composite exhibits a broad band at 443 cm^{-1} , which arises due to the Bi–O Raman stretching frequency.³⁶ The observed peak broadening in the Raman spectrum of the Bi_2O_3 in the lower-frequency region is attributed to the atomic disorder resulting from the random orientation of the lone-pair orbitals of Bi atoms.³⁶

To quantify the amount of carbon present in the CQD– Bi_2O_3 composite, thermogravimetric (TG) analysis was performed in the temperature range of 30 – $700\text{ }^{\circ}\text{C}$ under N_2 atmosphere. The TG profile shown in Figure S1 (Supporting Information) exhibits a decrease in the weight at $100\text{ }^{\circ}\text{C}$ owing to the dehydration of the water molecules that are trapped within the grains. In the temperature range of 250 – $450\text{ }^{\circ}\text{C}$, an appreciable weight loss of about 25% was observed, which could be attributed to the complete decomposition of the CQD present in the CQD– Bi_2O_3 nanostructure. It is noted that the weight loss remained constant beyond $600\text{ }^{\circ}\text{C}$, implying clearly that the nanocomposite is composed of 25% carbon. The TG profile of the pristine CQD was also recorded, and the obtained profile is shown in Figure S2. It is seen that the CQD has a large weight loss as high as 85% due to decomposition of carbon, confirming that the CQD is predominantly composed of carbon moieties.

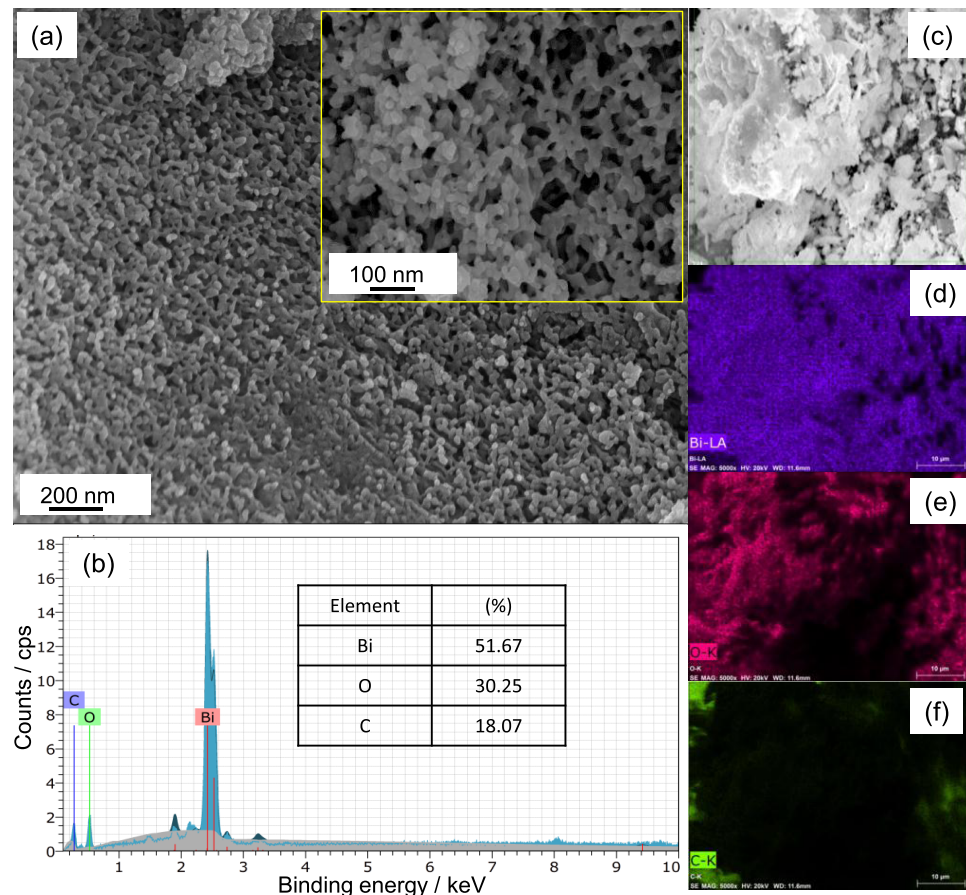


Figure 3. (a) FE-SEM images at various magnifications (inset), (b) EDX profile, and (c–f) elemental mappings performed on the surface of the CQD– Bi_2O_3 nanocomposite.

The formation of CQD– Bi_2O_3 involves several steps.^{28,37} In the initial step, under hydrothermal condition, the reaction between nitrate ion (NO_3^-) and water produces NH_3 and hydroxyl ion (OH^-) (eq 1). In the subsequent steps, the hydration of NH_3 leads to generation of ammonium ion (NH_4^+) and OH^- (eq 2). The formation of abundant OH^- increases the pH of the solution to yield unstable bismuth hydroxide ($\text{Bi}(\text{OH})_3$) (eq 3). The unstable ($\text{Bi}(\text{OH})_3$) undergoes decomposition to form stable Bi_2O_3 (eq 4). Prior to the formation of ($\text{Bi}(\text{OH})_3$), the addition of Bi^{3+} precursor to CQD solution resulted in the formation of CQD– Bi^{3+} intermediates, owing to the electrostatic interaction between the positively charged Bi^{3+} and negatively charged CQD. The negatively charged CQD seems to be displaced by OH^- to form $\text{Bi}(\text{OH})_3$. We have recently reported a similar strategy to prepare nanostructured MnO_2 and NiO , as reported elsewhere.^{28,37} The reactions leading to the formation of CQD– Bi_2O_3 are shown below



Figure 3a shows the field emission scanning electron microscopy (FE-SEM) images of the CQD– Bi_2O_3 composite acquired at different magnifications. It is obvious that the

morphology of the prepared material is characterized by uniform spherical particles of Bi_2O_3 grains with sparsely intertwined CQDs. The morphology of the CQD– Bi_2O_3 nanocomposite has the pore size in the range of 50–100 nm. Energy dispersive X-ray (EDX) analysis was carried out to establish the elements present in the sample, and the resultant EDX profile is depicted in Figure 3b. It is obvious that the peaks pertaining to bismuth, oxygen, and carbon are present. From the peak intensities of the EDX profile, the computed amounts of Bi, O, and C are 51.67, 30.25, and 18%, respectively. The determined amount of C in the sample almost agrees with the findings derived from TG analysis albeit with a slight difference. It is pertinent to note that the FE-SEM observations were performed by coating the sample onto a noncarbon substrate to get the exact amount of the carbon content in the material. The data obtained from the EDX analysis were further corroborated by elemental mappings as shown in Figure 3c–f. The elemental mappings clearly indicate the presence of all of the three elements (Bi, O, and C) with uniform distribution. Notably, the intensities of Bi and O are higher, implying that the prepared sample is primarily composed of Bi_2O_3 .

High-resolution transmission electron microscopy (HRTEM) images and the selected area electron diffraction (SAED) pattern of the CQD– Bi_2O_3 nanocomposite are shown in Figure 4. It is apparent that nanosized quasi-spherical Bi_2O_3 grains are enclosed within the carbon matrix with a clearly visible boundary separating both the Bi_2O_3 grains and the carbon (Figure 4a,b). The lattice fringe patterns of the

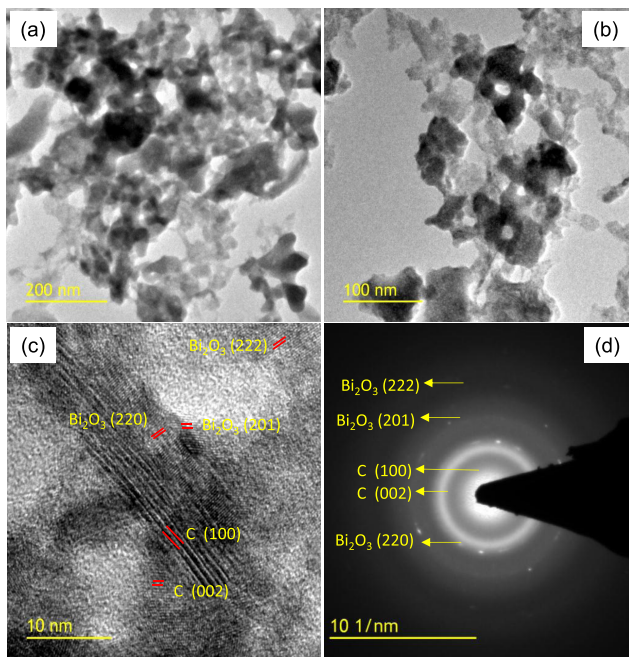


Figure 4. (a, b) TEM images, (c) lattice fringes, and (d) SAED pattern obtained for the CQD– Bi_2O_3 composite.

CQD– Bi_2O_3 nanocomposite sample are shown in Figure 4c. The presence of two-dimensional lattice fringes indicates the crystalline nature of the CQD– Bi_2O_3 nanocomposite. As evidenced from Figure 4c, the calculated d -spacing values from the lattice fringes 0.30, 0.26, and 0.16 nm are consistent with the (201), (220), and (222) planes of the Bi_2O_3 , respectively [JCPDS PDF # 65-1209].³⁴ However, the d -spacing values of 0.78 and 0.38 nm conform to the (100) and (002) planes of the carbon [JCPDS PDF # 75-1621], respectively.³⁵ As shown in Figure 4d, the SAED pattern is characterized by well-defined spots and rings. The presence of well-defined spots and rings in the SAED pattern further substantiates the crystalline nature of

the CQD– Bi_2O_3 nanocomposite. The computed d -spacing values from the SAED pattern are in good agreement with the d -spacing values of the Bi_2O_3 [JCPDS PDF # 65-1209] and carbon [JCPDS PDF # 75-1621], and this further complements the findings derived from the XRD analysis.

Performance of CQD– Bi_2O_3 as Anode for LIB. The Li-ion storage properties of the CQD– Bi_2O_3 anode were investigated by cyclic voltammetry (CV) and galvanostatic charge–discharge studies. Figure 5a shows the CV profiles obtained for the CR2032-type coin cell comprising the CQD– Bi_2O_3 as the anode and pure Li as the counter and reference electrodes in the voltage range of 0.01–3.0 V at a scan speed of 0.1 mV s^{−1}. It is apparent that in the first cycle, three prominent cathodic peaks are observed at 0.58, 1.3, and 1.5 V. The sharp peak at 0.58 V could be ascribed to the alloying reaction of Bi with Li to form Li_3Bi composition and the formation of solid electrolyte interface (SEI).^{13–17,37–39} The cathodic peak at 1.3 V is attributed to the reduction of the Bi_2O_3 and Li^+ leading to the formation of metallic Bi and Li_2O , whereas the peak centered at 1.5 V could be assigned to the reduction of tetragonal $\text{Bi}_2\text{O}_{2.33}$.^{13–17,38–40} The anodic part of the first cycle CV exhibits peaks at 1, 1.71, and 2.3 V. These peaks are attributed to dealloying of LiBi and Li_3Bi reactions and the subsequent oxidation reaction of Bi with Li_2O resulting in the regeneration of Bi_2O_3 .^{13–17,37–39} In the successive cycles, i.e., second and third cycles, it is pertinent to note that an additional peak appears at 0.74 V. The appearance of peaks in this region is associated with the simultaneous alloying reactions of Bi with Li to yield LiBi and Li_3Bi .^{13–17,38–40} It should be noted that in the first cycle, the cathodic peaks pertaining to the instantaneous alloying reactions are not observed owing to the formation of SEI near 1.0 V. Notably, the anodic peak observed at 1.71 V during the first cycle disappeared in the subsequent cycles, indicating that only a partial conversion has taken place between Bi_2O_3 and Bi.^{13–17,38–40} The CV curves showed an appreciable overlapping as we move from the second to the third CV sweep, indicating an excellent reversibility of the CQD– Bi_2O_3

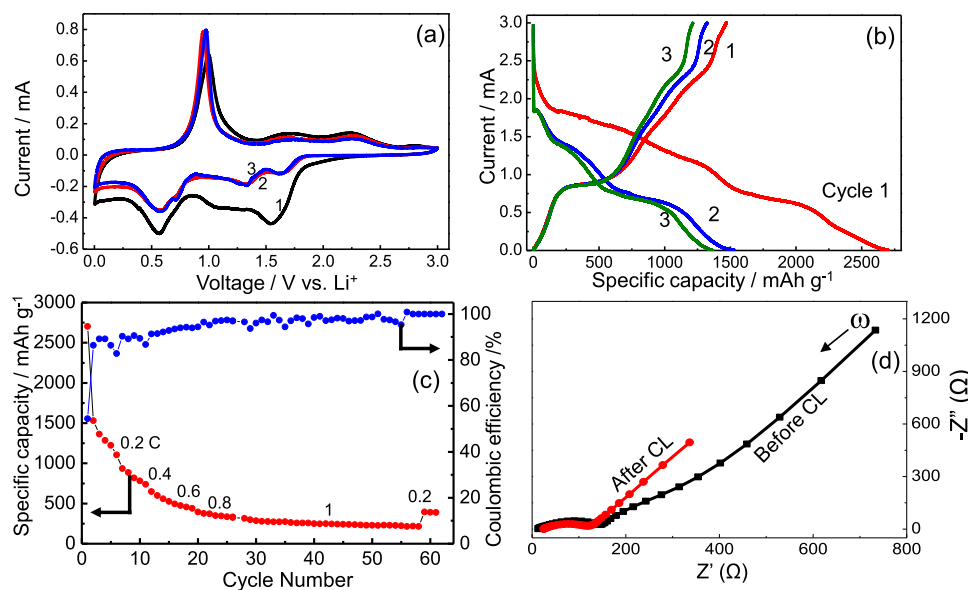
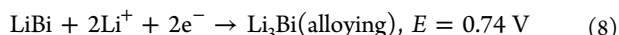
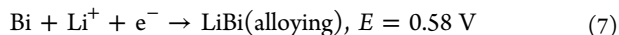
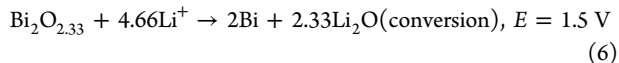
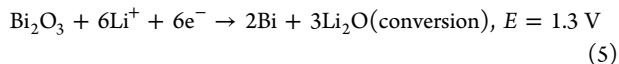


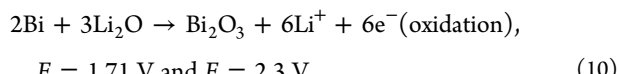
Figure 5. Cyclic voltammetry profiles at a scan rate of 0.1 mV s^{−1}, (b) galvanostatic charge–discharge curves cycled at 0.2C in the first three cycles, (c) cycle life data and coulombic efficiency obtained at different C rates, and (d) Nyquist plots obtained on the coin cell containing the CQD– Bi_2O_3 anode.

nanostructure toward alloying and dealloying. The various reactions that are associated with the Li storage in the CQD–Bi₂O₃ composite could be given as follows^{13–17}

Discharging



Charging



The observed CV characteristics of the CQD–Bi₂O₃ nanostructure are in good agreement with the previously reported works.^{13–17} Thus, it can be inferred that the as-prepared CQD–Bi₂O₃ nanostructure is electrochemically active and it has undergone simultaneous two-step alloying and conversion reactions with Li⁺ during the electrochemical reactions.

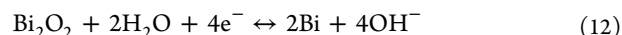
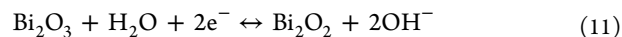
The charging and discharging performances of the CQD–Bi₂O₃ anode material were investigated in the potential range of 0.01–3.0 V at different current rates for 50 cycles. The representative charge–discharge profiles obtained on the coin cell at the 0.2C rate are displayed in Figure 5b. The obtained charge–discharge profiles are in good agreement with the above-discussed cyclic voltammetry studies of the CQD–Bi₂O₃ material. It can be noted that the initial discharge capacity of the CQD–Bi₂O₃ anode is about 2700 mA h g⁻¹. Such higher discharge capacity has been usually reported for the alternative anodes such as Si, Sn, Co₃O₄, etc.^{9,10} The higher discharge capacity could be ascribed to the formation of different lithiated phases as well as the simultaneous occurrence of conversion reaction and contribution from carbon (CQD).¹³ In the subsequent cycles, the discharge capacity dropped to 1500 mA h g⁻¹. Owing to the presence of the conductive carbon network, the as-prepared CQD–Bi₂O₃ anode material has retained a discharge capacity of 1200 mA h g⁻¹ after three cycles, which is much higher than the previously reported values for the bare Bi₂O₃, Bi₂O₃/rGO, and 3DOM β-Bi₂O₃ anode materials.^{14,17} Clear plateaus are observed during charging/discharging at potentials where redox peaks appeared in the CV curves, authenticating the occurrence of alloying/dealloying process. To examine the rate capability of the CQD–Bi₂O₃ anode material, cycle life data were acquired at different C rates, and the resultant data are shown in Figure 5c. The columbic efficiency was also noted at each C rate, and the calculated values are shown in Figure 5. It is observed that the increase in current rates has resulted in the decrease of discharge capacities. Such a decrease in discharge capacity arises due to rapid charge–discharge process and inefficient utilization of the active material. Remarkably, it can be seen from Figure 5c that the CQD–Bi₂O₃ anode exhibits discharge capacities of 2700, 935, 599, 394, and 298 mA h g⁻¹ at 0.2, 0.4, 0.6, 0.8, and 1C rates, respectively. Notably, at each C rate, a nearly stable discharge capacity is retained. For instance, at

0.6C rate, the discharge capacity is 599 mA h g⁻¹ and this capacity is nearly stable. The cycling stability recorded at 1C rate is separately given in Figure S4. It is seen that the CQD–Bi₂O₃ composite exhibits a stabilized discharge capacity of 300 mA h g⁻¹ for the examined 30 cycles with nearly 100% columbic efficiency.

It is noted that the preparation of CQD-anchored Bi₂O₃ composite resulted in a highly intertwined carbon network. The presence of carbon matrix around Bi₂O₃ grains could ensure excellent structural stability and offset the undesirable cracking of the electrode material by effectively accommodating the volume change associated with alloying/dealloying. Further, the presence of conductive carbon matrix could result in seamless electron/ion transports across the electrode/electrolyte and help in achieving stable SEI.^{41–43} Thus, the carbon nanonetwork has a profound influence on the overall electrochemical performance of the CQD–Bi₂O₃ composite.

To get further insight into the charge-transfer kinetics, impedance analysis was carried out on the as-assembled and cycled coin cells. The corresponding Nyquist plots in the frequency range of 400 kHz to 50 mHz are shown in Figure 5d. It is obvious that the impedance plot is characterized by the presence of a semicircle in the high-frequency region corresponding to electrode resistance and a straight line in the low-frequency range representing the Warburg element arising due to the diffusion-controlled charge-transfer process.⁹ It is apparent from Figure 5d that the diameter of the semicircle is almost invariant for the as-assembled and cycled coin cells. Interestingly, the presence of a steep slope in the low-frequency region indicates a rapid diffusion of Li⁺ ions into the anode material.⁹ Thus, from the electrochemical impedance spectroscopy (EIS), it can be inferred that the carbon matrix acted as a conductive network as well as a good support during the volume expansion of the metal oxide.

Supercapacitor Performances of CQD–Bi₂O₃. Initially, the supercapacitor characteristics of the CQD–Bi₂O₃ electrode were analyzed using CV and galvanostatic charge–discharge studies in a three-electrode configuration. Figure 6 shows the CV profiles recorded at different scan rates of 10, 20, 30, 50, and 100 mV s⁻¹ in 3 M KOH in the potential range of 0–0.8 V vs Ag/AgCl. It is obvious from Figure 6a that all of the CV profiles exhibit redox peaks, confirming the pseudocapacitance feature. The anodic peaks located at -0.12 and -0.32 V are ascribed to the oxidation of Bi to Bi²⁺ to form Bi₂O₂ metastable phase and oxidation of Bi²⁺ to Bi³⁺, while the prominent cathodic peak at -0.38 V is due to the reduction of Bi³⁺ to Bi²⁺ and subsequent formation of Bi (i.e., Bi₂O₃ ↔ intermediate Bi²⁺ (Bi₂O₂) ↔ Bi).^{21–23,44} It can be noted that at a higher scan speed, the CV profiles are characterized by increased current response along with a notable shift in the anodic and cathodic peak positions, which could be ascribed to structural changes or the IR drop.^{21–23} The increase in the peak current with increase of the scan rate signifies that the CQD–Bi₂O₃ electrode possesses excellent rate capabilities, which could result in fast quasi-reversible faradic reactions.^{21–23,25,28} The electrochemical reactions that are responsible for the appearance of redox peaks in KOH are given below^{21–23}



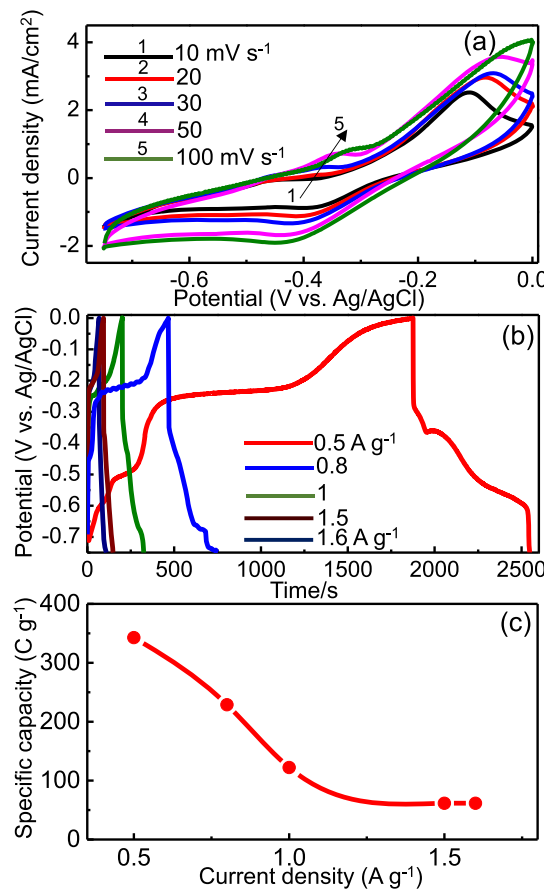


Figure 6. (a) Cyclic voltammetry curves of the CQD–Bi₂O₃ electrode at different scan rates, (b) galvanostatic charge–discharge profiles at different current densities, and (c) dependence of specific capacity on current density.

Galvanostatic charge–discharge profiles were recorded out to get further insights into the capacity characteristics of the CQD–Bi₂O₃ electrode. Figure 6b shows the charge–discharge profiles recorded in the potential range of −0.8 to 0 V at different current densities, 0.5, 0.8, 1, 1.5, and 1.6 A g⁻¹. It is pertinent to note that the obtained charge–discharge curves are nonsymmetric. The voltage drop at the initial stage of discharge is ascribed to the internal resistance of the CQD–Bi₂O₃ electrode. The plateau observed in the range 0.4–0.6 is ascribed to the faradic process owing to the CQD–Bi₂O₃.^{21–23} It is noted that the charge–discharge profiles are disproportionate, especially at lower current density. This results in a lower coulombic efficiency. Such lower coulombic efficiency at low current density could be due to phase change of Bi₂O₃ in CQD–Bi₂O₃, as has been reported previously by Shinde et al.²² In the subsequent cycling, Bi₂O₃ seems to be stabilized. It can be seen that at higher current density, the CQD–Bi₂O₃ nanocomposite has high coulombic efficiency.

The specific capacity of the CQD–MnO₂ electrode was calculated from the charge–discharge profiles using the following formula²⁸

$$C = I\Delta t/m \text{ C g}^{-1} \quad (14)$$

where C is the specific capacity (C g⁻¹), I is the discharge current (A), Δt is the discharge time (s), and m is the active mass of the electrode (g). The dependence of specific capacity on the applied current density is given in Figure 6c. It can be

inferred that with the increase of current density, the specific capacity showed a considerable decrease. At high current density, the rapid charging–discharging process would result in poor utilization of the active material, thereby resulting in low capacity. Such trends are often observed for battery-type materials.

The specific capacity of the CQD–Bi₂O₃ electrode estimated at 0.5 A g⁻¹ was as high as 343 C g⁻¹. It is observed that the CQD–Bi₂O₃ electrode exhibits a specific capacity of about 61 C g⁻¹ even at a higher current of 1.6 A g⁻¹. The specific capacitance value in the range 75–300 F g⁻¹ has been reported for the Bi₂O₃-based electrodes, as shown in Table S1. Notably, the CQD–Bi₂O₃ electrode exhibits better specific capacity compared to the reported values, indicating that the CQD–Bi₂O₃ can be a potential electrode for supercapacitor application.^{39,45} It is pertinent to note that the CQDs used in the preparation of the CQD–Bi₂O₃ composite resulted in an agglomerated intertwined carbon network across the Bi₂O₃ matrix, as has been confirmed by SEM and TEM. The absence of isolated CQD grains in the HR-TEM images further supports that the CQDs are composited with Bi₂O₃. In the composite, the diffusion path between the Bi₂O₃ grains are filled by the conductive CQD. Hence, the overall conductivity of the composite is enhanced by reducing the interfacial as well as grain boundary resistances that resulted in better electrochemical performance. To substantiate this, conductivity measurement was done for each of the CQD, Bi₂O₃, and CQD–Bi₂O₃ nanocomposite. The obtained conductivity profiles of the samples are displayed in Figure S3. It is seen that the frequency-independent dc conductivity is the lowest for the Bi₂O₃ and the highest for the CQD–Bi₂O₃ nanocomposite. The CQD exhibits higher conductivity than the Bi₂O₃. This observation clearly confirms that the CQD–Bi₂O₃ nanocomposite has resulted in much better electrochemical performance owing to the high conductivity, surface area, and quick electron/ion transportations.

Electrochemical impedance spectroscopy (EIS) studies were carried out on freshly prepared electrode as well as at the end of the 1000 charge–discharge cycles, and the obtained Nyquist plots are given in Figure 7. It is seen that both the plots comprise a depressed semicircle in the high-frequency region and an extended spike (Warburg element) in the low-frequency region. It is apparent that the Nyquist plot of the cycled electrode showed a significant decrease in the diameter of the semicircle and the Warburg element shifts to a lower

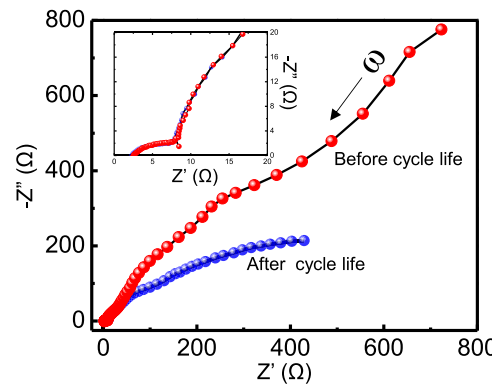


Figure 7. Nyquist plots recorded for the as-prepared and 2000-cycled CQD–Bi₂O₃ electrode in 3 M KOH.

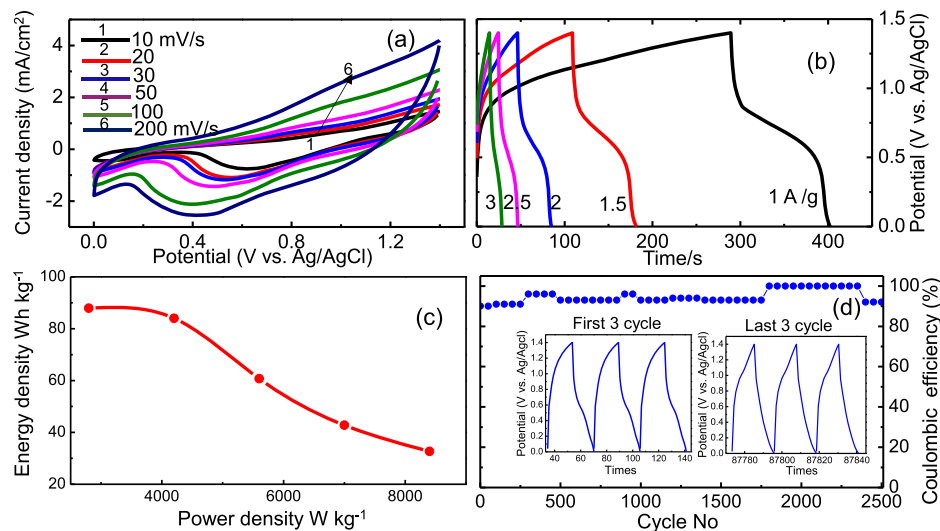


Figure 8. (a) Cyclic voltammograms of the asymmetric device at different scan rates, (b) galvanostatic charge–discharge profiles at different current densities, (c) Ragone plot, and (d) capacity retention data obtained at 2.50 A g⁻¹ for the CQD–Bi₂O₃ || KOH || rGO asymmetric device.

Table 1. Energy and Power Densities Reported for the Bi₂O₃-Based Asymmetric Supercapacitors

s. no.	material	method	energy density (Wh kg ⁻¹)	power density (W kg ⁻¹)	references
1	Bi ₂ O ₃	chemical precipitation	35	497	42
2	β-Bi ₂ O ₃	hydrothermal	32	5717	43
3	Bi ₂ O ₃ –Ni–F	chemical precipitation	11	720	22
4	Bi ₂ O ₃ nanowires	metal vapor transport deposition technique	138	1600	44
5	ESCNF@Bi ₂ O ₃	solvothermal	25	786	21
6	Bi ₂ O ₃ /MnO ₂ nanoflowers	solvothermal	11	352	49
7	CQD–Bi ₂ O ₃ composite	hydrothermal	32	8400	this work

resistance value. Remarkably, the resistance of the CQD–Bi₂O₃ electrode cycled up to 1000 cycles increased significantly, which may be due to degradation of the electrode material upon cycling. The presence of Warburg element suggests the existence of diffusion-controlled faradic reactions.^{25,28} Moreover, the inclination of the Warburg element to 45° toward x-axis clearly implies the dominance of the diffusion-controlled process.

Performance of Asymmetric Supercapacitor Device. To evaluate the practical applicability of the prepared CQD–Bi₂O₃ composite, asymmetric supercapacitor was constructed using the CQD–Bi₂O₃ as positive electrode and the rGO as negative electrode in 3 M KOH. The electrochemical behavior of the fabricated asymmetric device was evaluated in the potential range of 0–1.4 V. The CV curves of the asymmetric device at various scan rates of 10, 20, 30, 50, 100, and 200 mV s⁻¹ are shown in Figure 8a. It is evident that the CV profiles of the asymmetric device displayed a quasi-rectangular shape with redox peaks, and the operating cell voltage can be as high as 1.4 V. Such an enhanced operating voltage could significantly enhance the energy density of the device. It is to be noted that at all scan rates, the CV curves displayed both faradic (peak at 0.5 V) and nonfaradic contributions, confirming the perfect asymmetric supercapacitor behavior. With the increase of the scan rate, the anodic and cathodic currents showed a significant increase, which is characteristic of an ideal supercapacitor. Besides the obvious redox peaks in CV profiles, even at a higher scan rate of 200 mV s⁻¹, the electrode exhibits excellent rate capability in the fabricated device. The galvanostatic charge–discharge curves for the asymmetric device acquired at various current densities in 3 M KOH are

shown in Figure 8b. It can be seen in Figure 8b that the charge–discharge profiles exhibit a clear plateau in the voltage range of 0.6–0.4 V, substantiating the aforementioned CV data. The energy density and power density of the device were calculated using the following equations^{25,28}

$$E = 1/2 \times 3.6 CV^2 \text{ Wh kg}^{-1} \quad (15)$$

$$P = E \times 3600/\Delta t \text{ W kg}^{-1} \quad (16)$$

where E is the energy density (Wh kg⁻¹), C is the specific capacitance (F g⁻¹), V is the potential window (V), P is the power density (W kg⁻¹), and t is the discharge time (s). Figure 8c shows the Ragone plot obtained for the asymmetric device. It is seen that the fabricated asymmetric device achieved a maximum energy density of 88 Wh kg⁻¹ at a power density of 2799 W kg⁻¹, while the power density reached the highest value of 8400 W kg⁻¹ at the energy density of 32 Wh kg⁻¹. Such a high power density has not been reported for the Bi₂O₃-based device. Table 1 shows the reported energy and power densities for the Bi₂O₃-based asymmetric device.^{21,22,46–49} So far, Bi₂O₃-based asymmetric device exhibited energy density in the range of 13–130 Wh kg⁻¹ with power density in the range of 700–1600 W kg⁻¹. In the present work, it is evident that the fabricated asymmetric device consisting of the CQD–Bi₂O₃ delivers passable energy density with the highest power density. These results clearly imply that the fabricated asymmetric device hold great potentials for application in practical energy-storage systems. An ideal supercapacitor device must possess good long-term cycling stability. Thus, the cycle life data of the fabricated asymmetric device were

tested over 2500 cycles at 3 A/g (shown in Figure 8d). The charge–discharge profiles of the device obtained for the first and the last three cycles are displayed in the inset of Figure 8d. The unperturbed charge–discharge profiles during the cycle life imply excellent cycling stability. The average coulombic efficiency was as high as 95%. Remarkably, the fabricated device works at a high operating voltage window of 0–1.4 V, which is highly required for practical devices. Finally, the practical applicability of the CQD–Bi₂O₃ electrode was tested by fabricating an asymmetric device in the form of a coin cell with CQD–Bi₂O₃ as positive electrode and the rGO as negative electrode in 3 M KOH using Whatman filter paper as the separator. The fabricated device was charged to a potential of up to 1.4 V and discharged to glow commercial light-emitting diode (LED), as shown in Figure 9.

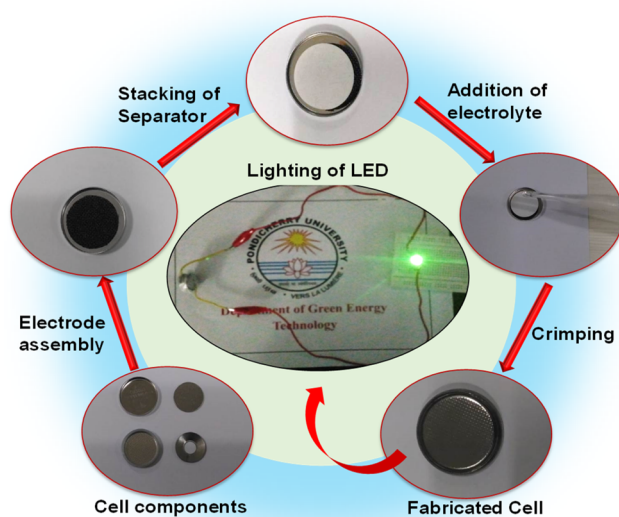


Figure 9. Photograph of various steps involved in the fabrication of the asymmetric supercapacitor device and the subsequent lighting of the LED.

CONCLUSIONS

In summary, we have demonstrated a simple and facile route to generate nanostructured CQD–Bi₂O₃ composite. The morphology of the composite consisted of uniform spherical particles of Bi₂O₃ with sparsely intertwined CQDs. The electrochemical studies revealed that the CQD–Bi₂O₃ anode has undergone simultaneous conversion and alloying reactions reversibly with Li. The fabricated coin cell composed of the CQD–Bi₂O₃ composite as anode material achieved a discharge capacity of 1500 mA h g⁻¹ at 0.2C with reasonable durability. The three-electrode supercapacitor studies revealed a battery-type pseudocapacitance behavior with a specific capacity of 343 C g⁻¹ at 0.5 A g⁻¹. The fabricated asymmetric device constructed using the CQD–Bi₂O₃ and rGO electrodes delivered excellent energy and power densities with a wide operating potential window of 0–1.4 V. The fabricated device retained almost 100% coulombic efficiency even in the 2500th cycle. We believe that the present study using CQD mediator offers new strategies for the development of a simple and multifunctional nanostructured carbon network metal oxide-based electrode material for energy-storage applications.

Further, the present synthesis strategy can be explored for preparing other metal oxide systems to use them in energy storage, photocatalysis, electrochemical water splitting, and other applications.

EXPERIMENTAL SECTION

Material Synthesis. The detailed preparation and characterizations of the CQDs have been reported in our recent works.^{28,50} Briefly, 25 mL of denatured waste milk was added to 20 mL of distilled water in a beaker. The resulting solution was transferred to a 50 mL Teflon-lined autoclave and heated at 160 °C for 2 h to yield CQD dispersions. The dark brown CQD dispersion was subjected to centrifugation (10 000 rpm) and subsequently freeze-dried to obtain CQD powder.

For preparation of CQD–Bi₂O₃, 1 g of Bi(NO₃)₃ was added to 3 mL of HNO₃ and 12 mL of distilled water and sonicated to dissolve the nitrate. To this solution, 0.1 g of solid CQD was added and the solution was made up to 25 mL by adding 12 mL of distilled water with brief sonication until the solution turns dark brown. The solution was then heated at 170 °C for 2 h in a Teflon-lined autoclave to yield a transparent yellow solution. The solution was further heated to dryness at 120 °C to yield solid yellow powder and used for further characterizations.

Material Characterizations. The X-ray diffraction (XRD) pattern of the as-prepared CQD–Bi₂O₃ composite was examined in the 2θ range of 10–75° at a scan speed of 1° per minute using a diffractometer (Bruker D8 PXRD) equipped with Cu Kα ($\lambda = 1.5184 \text{ \AA}$) radiation source. Fourier transform infrared (FT-IR) profiles were acquired using Nicolet 6700 by means of the KBr pellet method. Raman spectroscopy measurements were done using Witec Confocal Raman instrument with a 750 nm Ar ion laser. The surface morphology and chemical composition of the as-prepared material were analyzed by a field emission scanning electron microscope (FE-SEM Carl Zeiss SUPRA55VP) equipped with an energy-dispersive X-ray (EDAX) spectrometer. The particle size and morphology of the as-prepared CQD–Bi₂O₃ was examined using a high-resolution transmission electron microscope (JEOL JEM 2100) at an operating voltage of 200 kV. The absorption spectral analysis was carried out using a UV–visible spectrophotometer (Varian Cary-5000). The steady-state and time-resolved fluorescence decay profiles were recorded using a spectrofluorometer (HORIBA Jobin Yvon Fluorolog-FL3-11). The excitation source was a 450 W xenon lamp, and the samples were excited at a wavelength of 360 nm. For lifetime studies, pulsed nano-LED was used to excite the sample at 295 nm. Thermogravimetric analysis of the CQD–Bi₂O₃ was carried out in the temperature range of 30–700 °C in N₂ atmosphere at a 10 °C min⁻¹ scan rate by using a thermogravimetric analyzer (TG-DTA-Q 600 SDT). For conductivity measurement, each powder sample was made into 10 mm diameter pellets with thicknesses of 0.9 mm (CQD–Bi₂O₃), 3.5 mm (CQD), and 0.92 mm (Bi₂O₃). Then, the pellets were placed in between current collectors and impedance data were measured by using an impedance analyzer (Material Mates M2-7260). From the impedance data, the conductivity of the samples was estimated by using the following equation⁵¹

$$\sigma = (1/R) \cdot l / AS \text{ cm}^{-1} \quad (17)$$

where l is the thickness of the sample, A is the cross-sectional area of the pellet, and R is the resistance.

Fabrication of LIB and Electrochemical Characterization. The electrochemical measurements of the CQD– Bi_2O_3 composite were evaluated by fabricating CR2032-type coin cells that were assembled inside an Ar-filled glovebox (Nichwell α-1500u). Briefly, the anode was prepared by mixing 70 wt % active material (CQD– Bi_2O_3), 20 wt % super P carbon, and 10 wt % poly(vinylidene fluoride) (PVDF) binder in *N*-methyl-2-pyrrolidone solvent to yield a homogeneous slurry. The obtained slurry was then coated onto the Cu foil (9 μm thickness) by means of the doctor blade technique and subsequently vacuum-dried at 100 °C for 12 h. The active material-coated copper foil was cut into disks of 16 mm diameter and used as electrode. The mass of active material loaded onto the Cu foil was 2 mg. Pure Li disk was used as the counter and reference electrodes. LiPF_6 (1 M) in ethylene carbonate (EC)/dimethyl carbonate/diethyl carbonate (2:1:2 volume ratio) was used as the electrolyte, and Celgard was used as the separator. The cyclic voltammograms (CVs) were recorded on the fabricated coin cell in the potential range of 0.01–3.0 V at a scan rate of 0.1 mV s^{−1} using Biologic SP-150 workstation. The electrochemical impedance measurements were carried out on the coin cell in the frequency range of 400 kHz to 50 mHz by using the same electrochemical workstation. The galvanostatic charge–discharge cyclings were done on the coin cells at each of the 0.2, 0.4, 0.6, 0.8, and 1C rates using NEWARE (CT-3008) battery testing system.

Supercapacitor Fabrication and Testing. For the supercapacitor studies, the working electrode slurry was prepared by mixing CQD– Bi_2O_3 , carbon black, and poly(vinylidene fluoride) (PVDF) binder in the weight ratio of 70:20:10 using *N*-methyl-2-pyrrolidone (NMP) as the solvent. The obtained homogeneous slurry was pasted onto the carbon cloth (CC) substrate ($1 \times 1 \text{ cm}^2$) and dried overnight at 70 °C. Prior to the slurry coating, the CC was treated with conc. HNO_3 to make it a hydrophilic surface. A three-electrode cell was constructed using the working electrode, Pt as the counter electrode (area: $1 \times 1 \text{ cm}^2$), and Ag/AgCl as the reference electrode. All of the electrochemical studies were done in 3 M KOH. The cyclic voltammetry studies were done in the potential range of −0.75 to 0.0 V vs Ag/AgCl at different scan rates of 10, 20, 30, 50, and 100 mV s^{−1}. The galvanostatic charge–discharge profiles were recorded at different current densities of 0.5, 0.8, 1, 1.5, and 1.6 A g^{−1} in the same potential range. The electrochemical impedance of the electrode was obtained in the frequency range of 0.01–100 kHz with an excitation potential of 20 mV. All of the electrochemical characterizations were carried out using the same electrochemical workstation at room temperature (24 °C). The masses of the coated CC and the uncoated CC were measured using an electronic balance. From the difference in masses, the active mass of the electrode was found to be 1 mg.

■ ASSOCIATED CONTENT

S Supporting Information

The Supporting Information is available free of charge on the ACS Publications website at DOI: [10.1021/acsomega.8b03490](https://doi.org/10.1021/acsomega.8b03490).

TGA of the pristine and CQD– Bi_2O_3 nanocomposite, conductivity profiles, battery cycle life data of the CQD– Bi_2O_3 nanocomposite, and the comparison of the

supercapacitor performances of the Bi_2O_3 -based electrode materials ([PDF](#))

■ AUTHOR INFORMATION

Corresponding Author

*E-mail: elumalai.get@pondiuni.edu.in, drperumaleumali@gmail.com.

ORCID

Arumugam Selva Sharma: [0000-0002-1512-4546](#)

Perumal Elumalai: [0000-0002-2141-0047](#)

Notes

The authors declare no competing financial interest.

■ ACKNOWLEDGMENTS

E.D. acknowledges the Ministry of New and Renewable Energy, Govt. of India, for the National Renewable Energy fellowship (10/2(2) 2017). M.A. acknowledges the CSIR-UGC, Govt. of India, for junior research fellowship (JRF Grant No: 111424). A.S.S. acknowledges the Science and Engineering Research Board (SERB), Govt. of India, for the National Post-Doctoral Fellowship (PDF/2016/002815). PE thanks SERB, Government of India, for financial support (EMR/2016/001305) and CPRI-MoP (GDEC/2019). The authors acknowledge the Central Instrumentation Facility of Pondicherry University.

■ REFERENCES

- (1) González, A.; Goikolea, E.; Barrena, J. A.; Mysyk, R. Review on Supercapacitors: Technologies and Materials. *Renewable Sustainable Energy Rev.* **2016**, *58*, 1189–1206.
- (2) KarthikKiran, S.; Padmini, M.; Himadri, T. D.; Elumalai, P. Performance of Asymmetric Supercapacitor Using CoCr-Layered Double Hydroxide and Reduced Graphene-Oxide. *J. Solid State Electrochem.* **2016**, *21*, 927–938.
- (3) Peng, C.; Chen, B.; Qin, Y.; Yang, S.; Li, C.; Zuo, Y.; Liu, S.; Yang, J. Facile Ultrasonic Synthesis of CoO Quantum Dot/Graphene Nanosheet Composites with High Lithium Storage Capacity. *ACS Nano* **2012**, *6*, 1074–1081.
- (4) Winter, M.; Brodd, R. J. What are Batteries, Fuel Cells, and Supercapacitors? *Chem. Rev.* **2004**, *104*, 4245–4269.
- (5) Nitta, N.; Wu, F.; Lee, J. T.; Yushin, G. Li-Ion Battery Materials: Present and Future. *Mater. Today* **2015**, *18*, 252–264.
- (6) Guo, Y.; Li, H.; Zhai, T. Reviving Lithium-Metal Anodes for Next-Generation High-Energy Batteries. *Adv. Mater.* **2017**, *29*, No. 1700007.
- (7) Hassoun, J.; Bonaccorso, F.; Agostini, M.; Angelucci, M.; Betti, M. G.; Cingolani, R.; Gemmi, M.; Mariani, C.; Panero, S.; Pellegrini, V.; Scrosati, B. An Advanced Lithium-Ion Battery Based on a Graphene Anode and a Lithium Iron Phosphate Cathode. *Nano Lett.* **2014**, *14*, 4901–4906.
- (8) Erickson, E. M.; Ghanty, C.; Aurbach, D. New Horizons for Conventional Lithium Ion Battery Technology. *J. Phys. Chem. Lett.* **2014**, *5*, 3313–3324.
- (9) Duraisamy, E.; Das, H. T.; Gurunathan, P.; Ramesha, K.; Elumalai, P. [Co(salen)] Derived Co/ Co_3O_4 Nanoparticle@ Carbon Matrix as High-Performance Electrode for Energy Storage Applications. *J. Power Sources* **2017**, *344*, 103–110.
- (10) Prasath, A.; Elumalai, P. Extraction of Nanostructured SiO_2 from Glass Waste: A Potential Anode Source for Lithium–ion Batteries. *ChemistrySelect* **2016**, *1*, 3363–3366.
- (11) Ni, J.; Bi, X.; Jiang, Y.; Li, L.; Lu, J. Bismuth Chalcogenide Compounds Bi_2X_3 (X = O, S, Se): Applications in Electrochemical Energy Storage. *Nano Energy* **2017**, *34*, 356–366.
- (12) Fiordiponti, P.; Pistoia, G.; Temperoni, C. Behavior of Bi_2O_3 as a Cathode for Lithium Cells. *J. Electrochem. Soc.* **1978**, *125*, 14–17.

- (13) Li, Y.; Trujillo, M. A.; Fu, E.; Patterson, B.; Fei, L.; Xu, Y.; Deng, S.; Smirnov, S.; Luo, H. Bismuth oxide: A New Lithium-Ion Battery Anode. *J. Mater. Chem. A* **2013**, *1*, 12123–12127.
- (14) Li, Z.; Zhang, W.; Tan, Y.; Hu, J.; He, S.; Stein, A.; Tang, B. Three-Dimensionally Ordered Macroporous β - Bi_2O_3 with Enhanced Electrochemical Performance in a Li-Ion Battery. *Electrochim. Acta* **2016**, *214*, 103–109.
- (15) Fang, W.; Zhang, N.; Fan, L.; Sun, K. Bi_2O_3 nanoparticles Encapsulated by Three-dimensional Porous Nitrogen-Doped Graphene for High-Rate Lithium Ion Batteries. *J. Power Sources* **2016**, *333*, 30–36.
- (16) Fang, W.; Zhang, N.; Fan, L.; Sun, K. Preparation of Polypyrrole-Coated $\text{Bi}_2\text{O}_3@$ CMK-3 Nanocomposite for Electrochemical Lithium Storage. *Electrochim. Acta* **2017**, *238*, 202–209.
- (17) Deng, Z.; Liu, T.; Chen, T.; Jiang, J.; Yang, W.; Guo, J.; Zhao, J.; Wang, H.; Gao, L. Enhanced Electrochemical Performances of $\text{Bi}_2\text{O}_3/\text{rGO}$ Nanocomposite via Chemical Bonding as Anode Materials for Lithium Ion Batteries. *ACS Appl. Mater. Interfaces* **2017**, *9*, 12469–12477.
- (18) Liu, T.; Zhao, Y.; Gao, L.; Ni, J. Engineering $\text{Bi}_2\text{O}_3\text{-}\text{Bi}_2\text{S}_3$ Heterostructure for Superior Lithium Storage. *Sci. Rep.* **2015**, *5*, No. 9307.
- (19) Uddin, M. S.; Das, H. T.; Maiyalagan, T.; Elumalai, P. Influence of Designed Electrode Surfaces on Double Layer Capacitance in Aqueous Electrolyte: Insights from Standard Models. *Appl. Surf. Sci.* **2018**, *449*, 445–453.
- (20) Das, H. T.; Mahendraprabhu, K.; Maiyalagan, T.; Elumalai. Performance of Solid-state Hybrid Energy-storage Device using Reduced Graphene-oxide Anchored Sol-gel Derived Ni/NiO Nanocomposite. *Sci. Rep.* **2017**, *7*, No. 15342.
- (21) Li, L.; Zhang, X.; Zhang, Z.; Zhang, M.; Cong, L.; Pana, Y.; Lin, S. A Bismuth Oxide Nanosheet-Coated Electrospun Carbon Nanofiber Film: A Free-Standing Negative Electrode for Flexible Asymmetric Supercapacitors. *J. Mater. Chem. A* **2016**, *4*, 16635–16644.
- (22) Shinde, N. M.; Xia, Q. X.; Yun, J. M.; Singh, S.; Mane, R. S.; Kim, K. H. A Binder-Free Wet Chemical Synthesis Approach to Decorate Nanoflowers of Bismuth Oxide on Ni-foam for Fabricating Laboratory Scale Potential Pencil-type Asymmetric Supercapacitor Device. *Dalton Trans.* **2017**, *46*, 6601–6611.
- (23) Gujar, T. P.; Shinde, V. R.; Lokhande, C. D.; Han, S. H. Electrosynthesis of Bi_2O_3 Thin Films and their use in Electrochemical Supercapacitors. *J. Power Sources* **2006**, *161*, 1479–1485.
- (24) Zheng, F. L.; Li, G. R.; Ou, Y. N.; Wang, Z. L.; Su, C. Y.; Tong, Y. X. Synthesis of Hierarchical Rippled Bi_2O_3 Nanobelts for Supercapacitor Applications. *Chem. Commun.* **2010**, *46*, 5021–5023.
- (25) Duraisamy, E.; Das, H. T.; Selva Sharma, A.; Elumalai, P. Supercapacitor and Photocatalytic Performances of Hydrothermally-derived $\text{Co}_3\text{O}_4/\text{Coo}$ @ Carbon Nanocomposite. *New J. Chem.* **2018**, *42*, 6114–6124.
- (26) Chao, D.; Zhu, C.; Xia, X.; Liu, J.; Zhang, X.; Wang, J.; Liang, P.; Lin, J.; Zhang, H.; Shen, Z. X.; Fan, H. J. Graphene Quantum Dots Coated VO_2 Arrays for Highly Durable Electrodes for Li and Na Ion Batteries. *Nano Lett.* **2015**, *15*, 565–573.
- (27) Unnikrishnan, B.; Wu, C. W.; Chen, I. P.; Chang, H. T.; Lin, C. H.; Huang, C. C. Carbon dot-mediated synthesis of manganese oxide decorated graphene nanosheets for supercapacitor application. *ACS Sustainable Chem. Eng.* **2016**, *4*, 3008–3016.
- (28) Prasath, A.; Athika, M.; Duraisamy, E.; Selva Sharma, A.; Elumalai, P. Carbon-Quantum-Dot-derived Nanostructured MnO_2 and its Symmetrical Supercapacitor Performances. *ChemistrySelect* **2018**, *3*, 8713–8723.
- (29) Chen, R.; Shen, Z. R.; Wang, H.; Zhou, H. J.; Liu, Y. P.; Ding, D. T.; Chen, T. H. Fabrication of Mesh-like Bismuth Oxide Single Crystalline Nanoflakes and their Visible Light Photocatalytic Activity. *J. Alloys Compd.* **2011**, *509*, 2588–2596.
- (30) Zhang, L. S.; Wang, W. Z.; Yang, J.; Chen, Z. G.; Zhang, W. Q.; Zhou, L.; Liu, S. W. Sonochemical Synthesis of Nanocrystallite Bi_2O_3 as a Visible-Light-driven Photocatalyst. *Appl. Catal., A* **2006**, *308*, 105–110.
- (31) Liu, X.; Pan, L.; Lv, T.; Sun, Z.; Sun, C. Q. Visible Light Photocatalytic Degradation of Dyes by Bismuth Oxide-reduced Graphene Oxide Composites Prepared via Microwave-Assisted Method. *J. Colloid Interface Sci.* **2013**, *408*, 145–150.
- (32) Selva Sharma, A.; Ilanchelian, M. Comprehensive Multi-spectroscopic Analysis on the Interaction and Corona Formation of Human Serum Albumin with Gold/Silver Alloy Nanoparticles. *J. Phys. Chem. B* **2015**, *119*, 9461–9476.
- (33) Selva Sharma, A.; Ilanchelian, M. Elucidation of Photophysical Changes and Orientation of Acridine Orange Dye on the Surface of Borate Capped Gold Nanoparticles Using Multi-Spectroscopic Techniques. *Photochem. Photobiol. Sci.* **2014**, *13*, 1741–1752.
- (34) Pakhira, B.; Ghosh, M.; Allam, A.; Sarkar, S. Carbon nano onions cross the blood brain barrier. *RSC Adv.* **2016**, *6*, 29779–29782.
- (35) Ng, C. H.; Lim, H. N.; Hayase, S.; Zainal, Z.; Shafie, S.; Huang, N. M. Effects of Temperature on Electrochemical Properties of Bismuth Oxide/Manganese Oxide Pseudocapacitor. *Ind. Eng. Chem. Res.* **2018**, *57*, 2146–2154.
- (36) Betsch, R. J.; White, W. B. Vibrational Spectra of Bismuth Oxide and the Sillenite-Structure Bismuth Oxide Derivatives. *Spectrochim. Acta, Part A* **1978**, *34*, 505–514.
- (37) Mahendraprabhu, K.; Elumalai, P. Influence of precursors on formation of NiO nanostructures in hydrothermal synthesis. *Nanosci. Technol. Int. J.* **2015**, *73*, 428–433.
- (38) Wang, H.; Yang, H.; Lu, L. Topochemical Synthesis of Bi_2O_3 Microribbons Derived from a Bismuth Oxalate Precursor as High-Performance Lithium-Ion Batteries. *RSC Adv.* **2014**, *4*, 17483–17489.
- (39) Pistoia, G.; Pasquali, M.; Rodante, F. Button Cells Based on the $\text{Li}/\text{Bi}_2\text{O}_3$ couple. *J. Power Sources* **1985**, *16*, 263–269.
- (40) Khan, Z.; Bhattu, S.; Haram, S.; Khushalani, D. SWCNT/ BiVO_4 Composites as Anode Materials for Supercapacitor Application. *RSC Adv.* **2014**, *4*, 17378–17381.
- (41) Wang, P.; Zhang, Y.; Yin, Y.; Fan, L.; Zhang, N.; Sun, K. In Situ Synthesis of $\text{CuCo}_2\text{S}_4@\text{N/S-Doped}$ Graphene Composites with Pseudocapacitive Properties for High-Performance Lithium-Ion Batteries. *ACS Appl. Mater. Interfaces* **2018**, *10*, 11708–11714.
- (42) Zhang, Y.; Fan, L.; Wang, P.; Yin, Y.; Zhang, X.; Zhang, N.; Sun, K. Coupled flower-like Bi_2S_3 and graphene aerogels for superior sodium storage performance. *Nanoscale* **2017**, *9*, 17694–17698.
- (43) Zhang, Y.; Wang, P.; Yin, Y.; Zhang, X.; Fan, L.; Zhang, N.; Sun, K. Heterostructured SnS-ZnS@C hollow nanoboxes embedded in graphene for high performance lithium and sodium ion batteries. *Chem. Eng. J.* **2019**, *356*, 1042–1051.
- (44) Zuo, W.; Zhu, W.; Zhao, D.; Sun, Y.; Li, Y.; Liu, J.; Lou, X. W. D. Bismuth oxide: A Versatile High-Capacity Electrode Material for Rechargeable Aqueous Metal-Ion Batteries. *Energy Environ. Sci.* **2016**, *9*, 2881–2891.
- (45) Zheng, F. L.; Li, G. R.; Ou, Y. N.; Wang, Z. L.; Su, C. Y.; Tong, Y. X. Synthesis of Hierarchical Rippled Bi_2O_3 Nanobelts for Supercapacitor Applications. *Chem. Commun.* **2010**, *46*, 5021–5023.
- (46) Senthilkumar, S. T.; Kalai Selvan, R.; Ulaganathan, M.; Melo, J. S. Fabrication of $\text{Bi}_2\text{O}_3||\text{AC}$ Asymmetric Supercapacitor with Redox Additive Aqueous Electrolyte and Its Improved Electrochemical Performances. *Electrochim. Acta* **2014**, *115*, 518–524.
- (47) Ma, X.-J.; Wei-Bin, Z.; Ling-Bin, K.; Yong-Chun, L.; Long, K. β - Bi_2O_3 : An Underlying Negative Electrode Material Obeyed Electrode Potential over Electrochemical Energy Storage Device. *Electrochim. Acta* **2016**, *192*, 45–51.
- (48) Qiu, Y.; Fan, H.; Chang, X.; Dang, H.; Luo, Q.; Cheng, Z. Novel Ultrathin Bi_2O_3 Nanowires for Supercapacitor Electrode Materials with High Performance. *Appl. Surf. Sci.* **2018**, *434*, 16–20.
- (49) Xu, H. H.; Hu, X. L.; Yang, H. L.; Sun, Y. M.; Hu, C. C.; Huang, Y. H. Flexible Asymmetric Micro-Supercapacitors Based on Bi_2O_3 and MnO_2 Nanoflowers: Larger Areal Mass Promises Higher Energy Density. *Adv. Energy Mater.* **2015**, *5*, No. 1401882.

(50) Athika, M.; Prasath, A.; Duraisamy, E.; Sankar Devi, V.; Selva Sharma, A.; Elumalai, P. Carbon-quantum Dots Derived from Denatured Milk for Efficient Chromium-ion Sensing and Supercapacitor Applications. *Mater. Lett.* **2019**, 156–159.

(51) Cheruku, R.; Vijayan, L.; Govindaraj, G. Electrical relaxation studies of solution combustion synthesized nanocrystalline $\text{Li}_2\text{NiZrO}_4$ material. *Mater. Sci. Eng., B* **2012**, 177, 771–779.